THE JOURNAL OF PHYSICAL CHEMISTRY C

pubs.acs.org/JPCC Article

Interdependence of Oxygenation and Hydration in Mixed-Conducting (Ba,Sr)$FeO_{3-\delta}$ Perovskites Studied by Density Functional Theory

M. F. Hoedl, D. Gryaznov, R. Merkle,* E. A. Kotomin, and J. Maier

Cite This: *J. Phys. Chem. C* 2020, 124, 11780−11789 Read Online

ACCESS | Metrics & More | Article Recommendations | Supporting Information

ABSTRACT: Protonic−electronic mixed-conducting perovskites are relevant as cathode materials for protonic ceramic fuel cells (PCFCs). In the present study, the relation between the electronic structure and the thermodynamics of oxygen nonstoichiometry and hydration is investigated for $BaFeO_{3-\delta}$ and $Ba_{0.5}Sr_{0.5}FeO_{3-\delta}$ by means of density functional theory. The calculations are performed at the PBE + U level and yield ground-state electronic structures dominated by an oxygen-to-metal charge transfer with electron holes in the O 2p valence bands. Oxygen nonstoichiometry is modeled for $0 \le \delta \le 0.5$ with oxygen vacancies in doubly positive charge states. The energy to form an oxygen vacancy is found to increase upon reduction, i.e., decreasing concentration of ligand holes. The higher vacancy formation energy in reduced (Ba,Sr)$FeO_{3-\delta}$ is attributed to a higher Fermi level at which electrons remaining in the lattice from the removed oxide ions have to be accommodated. The energy for dissociative H_2O absorption into oxygen vacancies is found to vary considerably with δ, ranging from ≈−0.2 to ≈−1.0 eV in $BaFeO_{3-\delta}$ and from ≈0.2 to ≈−0.6 eV in $Ba_{0.5}Sr_{0.5}FeO_{3-\delta}$. This dependence is assigned to the annihilation of ligand holes during oxygen release, which leads to an increase in the ionic charge of the remaining lattice oxide ions. The present study provides sound evidence that p-type electronic conductivity and the susceptibility for H_2O absorption are antagonistic properties since both depend in opposite directions on the concentration of ligand holes. The reported trends regarding oxygenation and hydration energies are in line with the experimental observations.

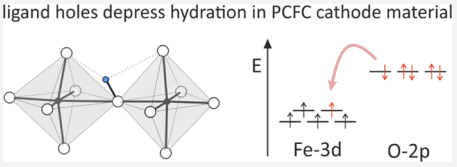

1. INTRODUCTION

The performance of protonic ceramic fuel cells (PCFCs) suitable for operation at intermediate temperatures of 400−600 °C has remarkably increased in recent years; see, e.g., refs 1−5. This progress can be largely attributed to improvements in the material choice and fabrication of the proton-conducting $Ba(Zr,Ce,Y,Yb)O_{3-\delta}$ electrolyte. In addition, cathode materials are optimized to enhance the reaction rate of the catalytic reduction of O_2 to H_2O. This is achieved by using mixed protonic/electronic conducting cathode materials that allow protons to migrate through the bulk of the cathode material and react with oxygen on its surface. By this means, the reactive zone for oxygen reduction is extended from the gas/cathode/electrolyte three-phase boundary to the entire gas−cathode interface. To activate this so-called "bulk path", a proton conductivity of roughly 10^{-5}−10^{-4} S/cm has been estimated to suffice.[6] Direct measurements of proton conductivity in cathode materials are extremely challenging, but proton concentrations have been determined for some perovskites.[3,7−14] Since cathode materials are redox-active, the proton uptake can occur either by a dissociative H_2O absorption into oxygen vacancies, $V_O^{\bullet\bullet}$, forming protonic defects $OH_O^{\bullet}$ (acid−base hydration reaction)

$$H_2O + O_O^x + V_O^{\bullet\bullet} \rightleftharpoons 2OH_O^{\bullet} \quad (1)$$

or by the hydrogenation reaction involving electron holes $h^{\bullet}$ (redox reaction)

$$H_2O + 2O_O^x + 2h^{\bullet} \rightleftharpoons 0.5O_2 + 2OH_O^{\bullet} \quad (2)$$

depending on ambient conditions.[14,15] In the present investigation, we focus on reaction (1), since this mode is generally investigated by thermogravimetry experiments. The degree of hydration, defined as the fraction of $V_O^{\bullet\bullet}$ filled by reaction (1), was found to be significantly lower for mixed-conducting perovskite cathode materials[13] compared to that for proton-conducting perovskite electrolyte materials.[16] This observation is not only relevant for the optimization of PCFC cathode materials but also imperative to understand their fundamental aspects. In addition to this overall trend, the degree of hydration varies strongly with the cation composition of the perovskite host.[13] So far, only a few theoretical studies have dealt with proton incorporation into PCFC cathode perovskites and related materials.[5,17−21] In particular, the

Received: March 4, 2020
Revised: April 28, 2020
Published: May 13, 2020

https://dx.doi.org/10.1021/acs.jpcc.0c01924
J. Phys. Chem. C 2020, 124, 11780−11789

dependence of hydration thermodynamics on the concentration of electron holes, which clearly shows up in experimental data,[13] has not yet been investigated by ab initio calculations. This is in contrast to unprotonated Fe and Co perovskites, for which the variation of $V_O^{\bullet\bullet}$ formation energies with hole concentration has been reported, e.g., in refs 22−24. For oxides without redox-active cations, a close relation of proton affinity and hydration enthalpy to the electronic structure has been discussed recently.[25]

Here, we focus on $BaFeO_{3-\delta}$ and $Ba_{0.5}Sr_{0.5}FeO_{3-\delta}$ perovskites, which exhibit comparably high degrees of hydration among cathode materials. The studied materials belong to the class of negative charge-transfer materials, in which the ground state is dominated by a $d^5\underline{L}$ configuration ($\underline{L}$: ligand hole).[26−29] Charge transfer occurs via Fe−O chemical bonds and is governed by their covalency. The extent of charge transfer therefore increases with the Sr content as the lattice contracts and the Fe 3d−O 2p hybridization increases.[27] In Krőger−Vink notation, the charge-transfer reaction can be expressed as

$$O_O^x + Fe_{Fe}^{\bullet} \leftrightarrow \{O_O^x - h^{\bullet}\} + Fe_{Fe}^x \quad (3)$$

where $Fe_{Fe}^{\bullet} = Fe^{4+}$ and $Fe_{Fe}^x = Fe^{3+}$. The electron hole formed by this reaction can be considered to be partially delocalized in the valence band. The presence of a Jahn−Teller (JT) distortion also depends on the extent of charge transfer since a distortion is expected for a d^4 (Fe^{4+}) configuration but is inhibited for a $d^5\underline{L}$ (Fe^{3+}) configuration.[28] Oxygen vacancy formation may then be expressed according to

$$O_O^x + 2h^{\bullet} \rightleftharpoons \frac{1}{2}O_2 + V_O^{\bullet\bullet} \quad (4)$$

While $BaFeO_{3-\delta}$ and $Ba_{0.5}Sr_{0.5}FeO_{3-\delta}$ experimentally show a rather high proton uptake, the presence of delocalized ligand holes prevents degrees of hydration as high as in electrolyte materials. However, no dependency of the hydration enthalpy on the degree of hydration itself, i.e., a proton−proton interaction, was experimentally observed.[30]

In the present investigation, we lay out the complex interplay of proton uptake and the concentration of ligand holes in $(Ba,Sr)FeO_{3-\delta}$ perovskites. We first analyze the unhydrated systems with perfect and oxygen-deficient stoichiometry regarding structural motifs and the thermodynamics of oxygen nonstoichiometry (Section 3.1). We then proceed to the protonated materials, where we analyze the O−H and O···H bond length distributions and report on hydration energies as a function of oxygen stoichiometry (Section 3.2).

2. METHODOLOGY

2.1. Computational Details. The density functional theory (DFT) calculations were carried out using the Vienna ab initio simulation package (VASP, v.5.4.4)[31−33] in conjuncture with the projector-augmented wave method.[34] The wave functions were expanded in terms of plane waves with a constant energy cutoff of 500 eV and were optimized with a break condition for the self-consistent loop of 10^{-5} eV.[34,35] Structural optimizations were performed until residual forces fell below 10^{-4} eV/Å. The Brillouin zone of the 5-atom primitive unit cell was sampled with an 8 × 8 × 8 Monkhorst−Pack k-point mesh.[36] We restrict the calculations to the high-spin ferromagnetic state and assume a homogeneous, strictly alternating distribution of Ba and Sr over the A-site of the perovskite lattice in the case of $Ba_{0.5}Sr_{0.5}FeO_{3-\delta}$.

Exchange−correlation was treated with the Perdew−Burke−Ernzerhof (PBE) functional[37] with an additional on-site Hubbard-U interaction term[38] for the Fe 3d states of U_{eff} = 4 eV. We explored U_{eff} ranging from 0 to 7 eV (cf. the Supporting Information) and found that U_{eff} = 4 eV represents a good compromise between reproducing experimental values, e.g., of the magnetic moment, and falling in the range of U_{eff} values typically employed for Fe-containing perovskites (see, e.g., refs 39−41).

Point defects were modeled using a 2 × 2 × 2 expansion of the primitive unit cell corresponding to a supercell of 40 atoms. The number of k-points in the supercells was reduced accordingly. All calculations were performed for neutral supercells with full relaxation of the supercell dimensions (allowing also for, e.g., monoclinic distortion) and of atomic coordinates. For the calculation of defect formation energies (see Section 2.2), defect-free $BaFeO_{3-\delta}$ and $Ba_{0.5}Sr_{0.5}FeO_{3-\delta}$ were also calculated in supercell form.

In cases of multiple point defects per supercell, different symmetry-independent arrangements are possible, which were generated with the supercell program.[42] Given the large number of supercells, which may contain several point defects and lack any symmetry elements, an efficient methodology for geometry and electronic structure optimization was required. We have therefore chosen a PBE + U approach over computationally much more demanding hybrid functionals.

Bader atomic charges were tested and found to be very sensitive toward structural distortions in the vicinity of point defects and are therefore not used for the discussion. Projection onto local atomic basis function and Mulliken population analyses have been carried out with the lobster code,[43−47] using Ba 5s 6s 5p, Sr 4s 5s 4p, Fe 4s 3p 3d, and O 2s 2p as valence band configurations. An evaluation of the obtained charges is provided in Section S2 of the Supporting Information.

2.2. Calculation of Thermodynamic Properties. The reaction energies $E_{V_O^{\bullet\bullet}}$ and E_{hydr} correspond to the energy change in reactions (4) and (1) and can be obtained through

$$\Delta E_{reac.} = E_{defect}^{tot} - E_{bulk}^{tot} + \sum_i \Delta n_i E_i \quad (5)$$

where E_i are the energies of the involved atomic species obtained from the total (DFT) energies of the respective O_2 and H_2O molecules, and Δn_i is the number of added or removed atomic species in the defective cell. To study nonideal behavior occurring at higher defect concentrations, we calculate the reaction energies as differential values. For example, eq 6 gives the formation energy of an oxygen vacancy in an already oxygen-deficient system. We will use a condensed notation to denote sum formulas hereafter, so that $O_{22} = (Ba,Sr)_8Fe_8O_{22}$

$$E_{V_O^{\bullet\bullet},O22} = E_{O22}^{tot} + E_{1/2O_2^{tot}} - E_{O23}^{tot} \quad (6)$$

The total energy of the O_2 molecule is not corrected for the notorious overestimation/underestimation of the binding energy/bond length obtained using the PBE functional, e.g., ref 40. The error in the total energy of O_2 causes an offset in the absolute values of $E_{V_O^{\bullet\bullet}}$ to higher values by ≈0.7 eV. The differential $E_{V_O^{\bullet\bullet}}$ is, however, unaffected by that error (Figure S2 in the Supporting Information).

The reaction energy of hydration, E_{hydr}, is calculated in a similar fashion according to the pure acid−base reaction (1).

https://dx.doi.org/10.1021/acs.jpcc.0c01924
J. Phys. Chem. C 2020, 124, 11780−11789

For example, eq 7 gives the hydration energy for an oxygen-deficient system containing two protons

$$E_{\mathrm{hydr,O23H2}} = E^{\mathrm{tot}}_{\mathrm{O23H2}} - E^{\mathrm{tot}}_{\mathrm{O22}} - E^{\mathrm{tot}}_{\mathrm{H_2O}} \quad (7)$$

For singly protonated supercells, we average over two unhydrated supercells, exemplified in eq 8. This reaction then corresponds to the hydration of an O22.5 supercell

$$E_{\mathrm{hydr,O23H1}} = 2E^{\mathrm{tot}}_{\mathrm{O23H1}} - E^{\mathrm{tot}}_{\mathrm{O22}} - E^{\mathrm{tot}}_{\mathrm{O23}} - E^{\mathrm{tot}}_{\mathrm{H_2O}} \quad (8)$$

In cases of more than one symmetry-independent arrangement of point defects in the supercell, e.g., O22 or O23H1, we average over the three lowest-energy configurations. A list of the configurations used for the calculation of $E_{V_O^{\bullet\bullet}}$ and E_{hydr} is given in Section S4 of the Supporting Information.

2.3. General Considerations on the (Ba,Sr)$FeO_{3-\delta}$ Crystal Structure. With a Goldschmidt tolerance factor exceeding 1, $BaFeO_{3-\delta}$ crystallizes in a hexagonal perovskite structure with face-sharing FeO_6 octahedra. Upon increasing the $V_O^{\bullet\bullet}$ concentration, $BaFeO_{3-\delta}$ is subject to a phase transformation into a pseudo-cubic perovskite phase with corner-sharing octahedra[48,49] and, ultimately, into a vacancy-ordered monoclinic perovskite phase.[50,51] This phase is, however, not isostructural with the Brownmillerite phase found for $Sr_2Fe_2O_5$ but has a more complex structure.[50,52] Fully oxidized metastable $BaFeO_3$ with corner-sharing octahedra can be prepared by the low-temperature oxidation of $BaFeO_{2.5}$.[53] In this form, the material adopts a cubic symmetry and does not exhibit any Jahn−Teller (JT) distortions. The cubic perovskite phase can, alternatively, be stabilized by slight doping with, e.g., 0.05 La or Ce on the Ba site,[54,55] bringing the Goldschmidt tolerance factor closer to 1. Instead, $Ba_{0.5}Sr_{0.5}FeO_{3-\delta}$ has a Goldschmidt tolerance factor closer to 1 and thus always adopts the perovskite cubic phase.[56] To keep $BaFeO_3$ and $Ba_{0.5}Sr_{0.5}FeO_{3-\delta}$ calculations comparable to each other, and to experimental reaction enthalpies that are typically reported on (doped) pseudo-cubic phases, we here use a cubic input geometry with corner-sharing octahedra for both compositions and then allow for relaxation of ionic positions and supercell dimensions.

In our calculations, some configurations containing Fe in 4-fold coordination yielded lower total energies after structural optimization than the lowest-energy configuration with only 5- or 6-fold coordination. This can be rationalized by $BaFeO_{3-\delta}$ favoring the phase with ordered $V_O^{\bullet\bullet}$, leading to 4- and 6-fold-coordinated Fe. We deliberately omit configurations with 4-fold-coordinated Fe in the present analysis because (i) ordered superstructures are not found experimentally for doped $BaFeO_{3-\delta}$ perovskites at elevated temperatures where $V_O^{\bullet\bullet}$ and proton concentrations are measured and (ii) it would lead to a spurious energy contribution from the phase transformation into the reaction energies.

3. RESULTS AND DISCUSSION

3.1. Unhydrated (Ba,Sr)$FeO_{3-\delta}$. Regarding the fully oxidized, perfect $BaFeO_3$, we find that the ground-state structure is characterized by a slight distortion of the FeO_6 octahedra. Each iron has Fe−O bond lengths of 2 × 1.89, 2 × 1.99, and 2 × 2.17 Å. These octahedra are connected such that along the *z*-direction, all Fe−O lengths are identical (1.99 Å, one of the short axes of the octahedra), while in the *x*- and *y*-directions, the other short axis (2 × 1.89 Å) and the long axis (2 × 2.17 Å) of the octahedra alternate (Figure 1, inset). This distortion pattern, interpreted as the hallmark of a cooperative Jahn−Teller (JT) effect, lowers the total energy by 0.02 eV per formula unit of $BaFeO_3$.

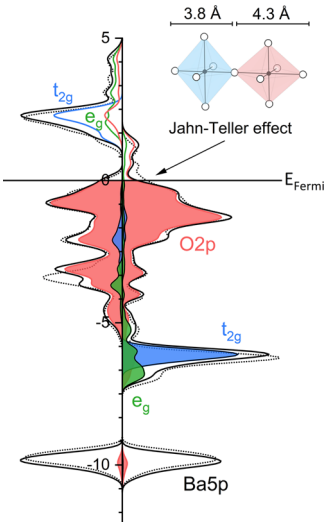

Figure 1. Projected density of states (P-DOS) of $BaFeO_3$, relative to the Fermi level (red: O 2p states, blue: t_{2g} states, green: e_g states). The black dashed line represents the DOS of the ideal, nondistorted structure. A snippet of the Jahn−Teller distortion pattern is shown as the inset (*z*-axis pointing into the paper plane).

In $Ba_{0.5}Sr_{0.5}FeO_{3-\delta}$, the JT distortion becomes negligible, and in $SrFeO_3$, with an even smaller lattice parameter, JT distortions are completely absent.[57] The trend of the fading JT distortion with the Sr content could be explained by the electronic structure favoring a $d^5\underline{L}$ state (Fe^{3+}) as the lattice parameter decreases and the Fe 3d−O 2p hybridization increases.[a]

The projected density of states (P-DOS) of $BaFeO_3$ is depicted in Figure 1. The Fe 3d spin-up and spin-down states are separated considerably, with the Fe 3d spin-up states lying below the O 2p valence band. While the t_{2g} bands are narrow and thus fairly localized, the e_g states are more dispersed, indicating a certain hybridization with the O 2p band. Although the e_g spin-up band is rather broad and extends far into the valence band, it is almost entirely filled and thus represents a $d^5\underline{L}$ situation. The ligand hole appears in the form of empty states in the spin-up O 2p band above the Fermi level. Given the presence of a small band gap in the spin-down channel slightly above the Fermi level, the material may be considered half-metallic. Based on the analysis of the P-DOS, we conclude that $BaFeO_3$ is a charge-transfer-type half-metal with electron holes in the O 2p spin-up valence band. The symmetry breaking induced by the JT distortion affects the Fe−O bonding characteristics and causes a subtle band splitting in the upper valence band, thereby reducing the density of states at the Fermi level. This is illustrated by superimposing the DOS of a nondistorted structure in Figure 1 as a dashed black line.

Substituting half of the A-site cations with Sr only mildly affects the crystal and electronic structures. The smaller ionic radius of Sr^{2+} as compared to that of Ba^{2+} leads to a smaller lattice constant and therefore a stronger Fe 3d−O 2p hybridization. As a result, the crystal as a whole becomes stiffer, and JT distortions become negligible in $Ba_{0.5}Sr_{0.5}FeO_{3-\delta}$.

https://dx.doi.org/10.1021/acs.jpcc.0c01924
J. Phys. Chem. C 2020, 124, 11780−11789

Table 1. Pseudo-Cubic Lattice Constant a, Fe Magnetic Moment μ_{Fe}, and Mulliken Atomic Charges Q of the Fully Oxidized and Reduced Systems

	a (Å)	a^{exp} (Å)	μ_{Fe} (μ_B)	μ_{Fe}^{exp} (μ_B)	Q_M^{Fe} (e)	Q_M^{O} (e)	Q_M^{Ba} (e)	Q_M^{Sr} (e)
$BaFeO_3$	4.04	3.97[53]	3.8	3.5[53]	1.65	−1.13	1.73	
$Ba_{0.5}Sr_{0.5}FeO_3$	3.96		3.8		1.68	−1.13	1.81	1.61
$BaFeO_{2.5}$	4.07		4.2		1.60	−1.32	1.70	
$Ba_{0.5}Sr_{0.5}FeO_{2.5}$	4.01	3.93[59]	4.2		1.62	−1.32	1.79	1.58

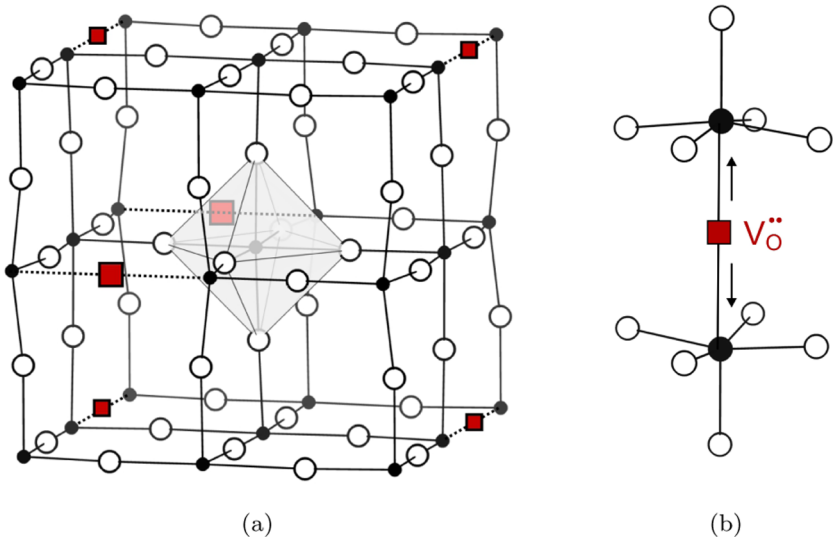

Figure 2. Crystal structure of oxygen-deficient $BaFeO_{3-\delta}$ (white spheres: O, black spheres: Fe, red squares: $V_O^{\bullet\bullet}$, Ba omitted, one $[FeO_6]$ coordination polyhedron shown as an example). (a) Disordered arrangement of $V_O^{\bullet\bullet}$ in $Ba_8Fe_8O_{22}$ and (b) typical structural motif of two distorted square pyramidal $[FeO_5]$ units connected by a $V_O^{\bullet\bullet}$.

Table 1 summarizes the calculated data for the fully oxidized and fully reduced systems, together with experimental data. Fe magnetic moments are obtained from the difference of the iron spin-up and spin-down integrated P-DOS. The calculated lattice constant and magnetic moments are in good agreement with the reported experimental values. Also, the negative charge transfer is in line with X-ray spectroscopy experiments.[26−29] The presence of ligand holes in the O 2p band together with the Fe 3d−O 2p hybridization reduces the O ion charge as compared to that of closed-shell perovskites with a similar lattice constant (compare −1.13e of $BaFeO_3$ versus −1.24e in cubic $BaTiO_3$ with a similar lattice constant of 3.99 Å).

As an example for an oxygen-deficient supercell, Figure 2a shows the structure of $Ba_8Fe_8O_{22}$. The $V_O^{\bullet\bullet}$ are arranged in a disordered way, being mutually separated by 4.9 Å. No correlation between the total energy and the $V_O^{\bullet\bullet}$−$V_O^{\bullet\bullet}$ distances was observed (Figure S4 in the Supporting Information). This indicates that the charge of the $V_O^{\bullet\bullet}$ is sufficiently screened by the rather delocalized valence band electrons, thus avoiding pronounced electrostatic interactions. Figure 2b shows a typical relaxation pattern in the vicinity of a $V_O^{\bullet\bullet}$. The two Fe ions are shifted away from the vacant site by about 0.15 Å, owing to the electrostatic repulsion in the absence of the connecting oxide ion, resulting in bent O−Fe−O. The outward displacement is compensated by shortening of the Fe−O bond opposite to the $V_O^{\bullet\bullet}$ (Figure S5: the shortest Fe−O distance in $[FeO_5]$ is significantly smaller than the shortest Fe−O distance in $[FeO_6]$ for the same oxygen stoichiometry) and further lattice distortions.

In each supercell, one can usually recognize 2−3 types of Fe atoms (1−2 for 6-fold-coordinated and 1−2 for 5-fold-coordinated Fe) with a characteristic distribution of Fe−O bond lengths and averaged Fe−O distance around this Fe ion. Figure 3 shows how these averaged Fe−O bond lengths evolve with increasing oxygen deficiency (extracted from fully optimized supercells, each symbol representing the Fe−O length averaged over the Fe−O (5-fold) and Fe−O (6-fold) polyhedra in the respective configuration). In a situation of

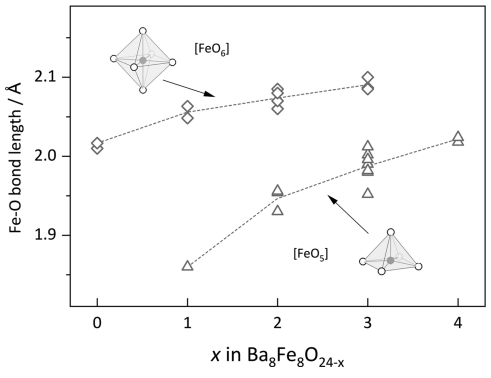

Figure 3. Average Fe−O bond length of $[FeO_5]$ and $[FeO_6]$ polyhedra in $BaFeO_{3-\delta}$ as a function of the increasing oxygen nonstoichiometry. Each symbol represents the average Fe−O length in Fe−O (5-fold) and Fe−O (6-fold) polyhedra (1−2 distinct FeO_5 and FeO_6 polyhedra per supercell). Data for $[FeO_5]$ and $[FeO_6]$ polyhedra from the three lowest configurations for each O stoichiometry are shown.

https://dx.doi.org/10.1021/acs.jpcc.0c01924
J. Phys. Chem. C 2020, 124, 11780−11789

strictly localized Fe oxidation states, one would expect a stepwise change of Fe−O distances when the central Fe changes from Fe^{4+} to Fe^{3+}, i.e., from a $[FeO_6]$ to $[FeO_5]$ polyhedron. However, for both types of polyhedra, the average Fe−O bond length increases smoothly with increasing oxygen deficiency. This clearly indicates a partial delocalization of electron holes. Annihilation of these holes during oxygen excorporation alters the oxide ions' charge density in both coordination polyhedra and, hence, induces a gradual change in the average Fe−O bond lengths. This is in line with the P-DOS discussed above (Figure 1) and makes a clear assignment of individual Fe oxidation states questionable. However, the JT distortion of $[FeO_6]$ octahedra characteristic of a d^4 (Fe^{4+}) configuration is partly preserved during the reduction, as evidenced by the broad distribution of Fe−O within $[FeO_6]$ octahedra; see Figure S5 in the Supporting Information. Therefore, we conclude that the ground state exhibits minor d^4 features like the JT distortions despite the dominating $d^5\underline{L}$ configuration.

The increased Fe−O bond length is also reflected in an overall lattice expansion as expressed by the pseudo-cubic lattice constant. Figure 4 shows the evolution of the pseudo-cubic lattice constant as a function of the oxygen non-stoichiometry for $BaFeO_{3-\delta}$ and $Ba_{0.5}Sr_{0.5}FeO_{3-\delta}$. Both systems are subject to a linear increase in lattice constant with increasing $V_O^{\bullet\bullet}$ concentration. The volumetric expansion is 9% per $\Delta\delta$ = 1 for $BaFeO_{3-\delta}$ and 7.6% per $Ba_{0.5}Sr_{0.5}FeO_{3-\delta}$. Comparable slopes have been reported for other systems. For instance, a slope of 14% for $La_{0.5}Sr_{0.5}FeO_{3-\delta}$ was found in a DFT study,[17] and a slope of 11% for $SrFe_{0.75}Ti_{0.25}O_{3-\delta}$ and $La_{0.3}Sr_{0.7}FeO_{3-\delta}$ was found in experimental studies.[60,61] The fact that these values are larger than those found in this study may be rationalized by the two materials $BaFeO_{3-\delta}$ and $Ba_{0.5}Sr_{0.5}FeO_{3-\delta}$ having Goldschmidt tolerance factors larger than 1 (1.072 and 1.042) so that the effective size increase upon reduction can at least partially be compensated without lattice expansion. In general, during oxygen depletion and reduction, according to reaction (4), two processes occur that can alter the materials' volume: (i) doubly charged $V_O^{\bullet\bullet}$ are smaller than regular oxide ions, which would result in a net contraction of the lattice if they were compensated by an artificial background charge used in DFT calculations;[62] and (ii) the annihilation of holes previously shared between Fe and O increases the size of the oxide ions. Since the holes were largely in oxygen states (Figure 1), hole annihilation changes the charge of O more than that of Fe (Table S1 in the Supporting Information; the same trend for Mulliken and Bader charges). Thus, the size of Fe and O ions is expected to increase, however, with a much larger contribution from oxygen. The fact that an overall expansion is observed means that process (ii) causes larger volume changes.

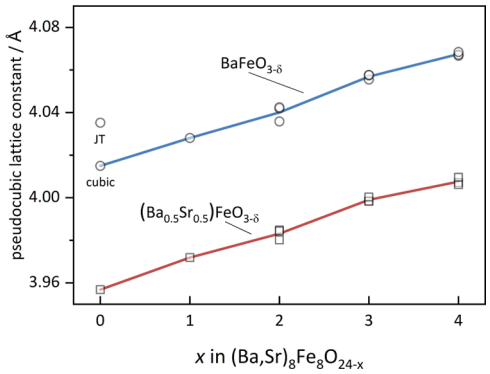

Figure 4. Evolution of the pseudo-cubic lattice constant of $(Ba,Sr)FeO_{3-\delta}$ upon increasing the oxygen deficiency. The line represents the average of the three lowest-energy configurations.

The total energy of oxygen-deficient supercells and the energy of the oxygen removed to the gas phase is plotted in Figure 5 as a function of the $V_O^{\bullet\bullet}$ concentration. In a system behaving ideally dilute, the energy would increase linearly. However, Figure 5 clearly shows that the energy increases nonlinearly with increasing oxygen deficiency or, equivalently, decreasing hole concentration. This corresponds to an increase of the differential vacancy formation energy (Figure 5, inset) and is qualitatively in line with the thermogravimetry experiments for $Ba_{0.95}La_{0.05}FeO_{3-\delta}$.[30,63] These experiments show the strongest deviation from ideal behavior at high oxygen partial pressure and comparably low T, i.e., under conditions with a high hole concentration.

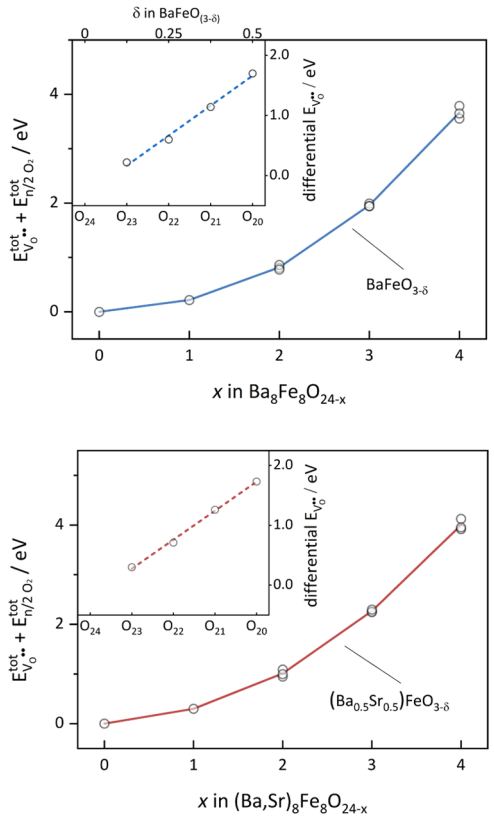

Figure 5. Total energy of the oxygen-deficient supercell and the energy of removed oxygen ($n/2$ O_2 in the gas phase for O24-n supercell) relative to the perfect O24 cell plotted as a function of the $V_O^{\bullet\bullet}$ concentration. The lines represent the average of the three lowest-energy configurations. The insets give the differential vacancy formation energy, $E_{V_O^{\bullet\bullet}}$.

Thus, we assign the observed nonideal behavior shown in Figure 5 rather to the variation of the hole concentration and their mutual interaction than to $V_O^{\bullet\bullet}$−$V_O^{\bullet\bullet}$ defect interactions. In the case of strong $V_O^{\bullet\bullet}$−$V_O^{\bullet\bullet}$ interactions disfavoring further $V_O^{\bullet\bullet}$ formation, the strongest deviation from ideal behavior would be expected at high $V_O^{\bullet\bullet}$ concentration (low pO_2, high T). The insets of Figure 5 depict the differential $V_O^{\bullet\bullet}$ formation energies (i.e., the energy increments required to stepwise

https://dx.doi.org/10.1021/acs.jpcc.0c01924
J. Phys. Chem. C 2020, 124, 11780−11789

remove the first, second, third, and fourth O from the 40-atom supercells). The values of $E_{V_O^{\bullet\bullet}}$ change with the hole concentration approximately linearly and are rather similar for $BaFeO_{3-\delta}$ and $Ba_{0.5}Sr_{0.5}FeO_{3-\delta}$. Their slopes are approximately 1.6 eV per hole (from formal Fe^{4+} to Fe^{3+}). The qualitative trend of decreasing $E_{V_O^{\bullet\bullet}}$ with increasing hole concentration agrees with the experimental results[63] and previous calculations on $Ba_{0.5}Sr_{0.5}Co_{1-y}Fe_yO_{3-\delta}$.[24] Hence, the characteristic deviations from ideally dilute defect chemistry already observed in the unhydrated systems are confirmed in the present DFT calculations. Experimentally, the oxygen partial molar enthalpy of $Ba_{0.85}La_{0.15}FeO_{3-\delta}$ (corresponding to $E_{V_O^{\bullet\bullet}}$; cf. Section 3.3) is found to change from −0.8 eV for zero hole concentration to −0.4 eV for 0.5 hole per formula unit,[63] which corresponds to a smaller slope (0.8 eV/hole) than the present DFT result. However, the data is limited to 0−0.5 holes per formula unit and comes with an experimental uncertainty in the range of 0.1 eV. The remaining quantitative deviation might be attributed to the large sensitivity of redox energetics on the employed DFT functional, which determines the degree of hole (de)localization.

We assign the observed nonideal behavior in $E_{V_O^{\bullet\bullet}}$ to the largely delocalized nature of the holes in the O 2p valence band. The DOS of oxidized and reduced $BaFeO_{3-\delta}$ is shown in Figure 6a,b. The energy levels are aligned to a common vacuum level obtained through separate slab calculations (see Section S7 in the Supporting Information). For the fully oxidized O24 cell (formal Fe^{4+} oxidation state), one can recognize empty O 2p states above the valence band maximum that correspond to the ligand hole at the O ions. Upon reduction to the O20 cell (formal Fe^{3+} oxidation state), these states become occupied and the work function decreases. The changes upon reduction are also reflected in the Mulliken atomic charges of Fe and O (Table 1). The Mulliken charge of O becomes more negative upon reduction from −1.13*e* in the O24 fully oxidized cell to −1.32*e* in the O20 fully reduced cell.

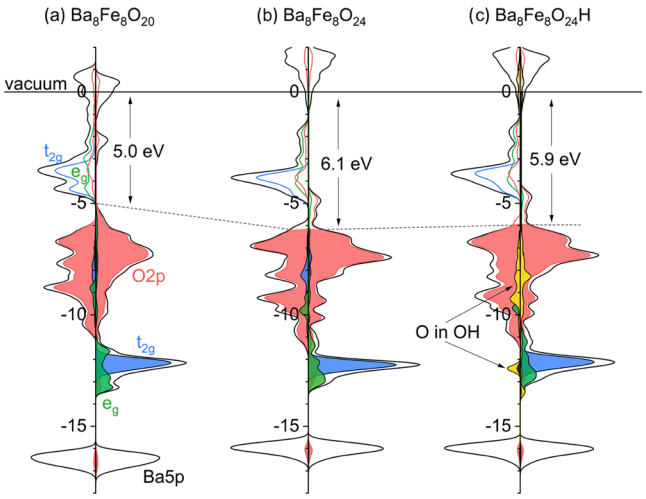

Figure 6. Electronic density of states of fully oxidized (O24), reduced (O20), and protonated (O24H) $Ba_8Fe_8O_{24-\delta}H_x$ cells relative to a common vacuum level. O-in-OH states, marked in yellow, are multiplied by a factor of 4 for better visibility. The band alignment procedure is outlined in the Supporting Information. The solid line indicates the common vacuum level, and the dashed line indicates the position of the highest occupied state.

The Fe Mulliken atomic charge is less affected by the reduction and changes only by 0.06*e*. The increase of $E_{V_O^{\bullet\bullet}}$ with increasing oxygen nonstoichiometry is a consequence of the increasing Fermi level (relative to the center of gravity of the O 2p states) because electrons remaining in the lattice from the removed oxide ions have to be accommodated at a higher energy level; cf. also.[64,65] Also, the small shift of the entire O 2p valence band to higher absolute energy contributes to it.

The present changes of $E_{V_O^{\bullet\bullet}}$ with increasing oxygen nonstoichiometry for $(Ba,Sr)FeO_{3-\delta}$ are of comparable magnitude as those calculated for $SrFeO_{3-\delta}$ in ref 22. However, given the issues with Bader atomic charges and the predominant O 2p character of the valence band, we rather refrain from assigning localized polarons to specific Fe atoms close to or more distant to the $V_O^{\bullet\bullet}$, as done in refs 22, 23.

3.2. Hydrated $(Ba,Sr)FeO_{3-\delta}$. Proton interstitials occupy a position close to an oxide ion, thus forming a covalent bond. The length of this bond falls in the range of 0.97−1.01 Å and is thus much shorter than the oxide ion radius of 1.4 Å, i.e., the proton becomes completely immersed in the oxide ion's electron cloud. The bond lengths found in $(Ba,Sr)FeO_{3-\delta}$ are similar to those calculated for $(La,Sr)FeO_3$[17] and $BaZrO_3$.[66] The formation of the OH covalent bond leads to a stabilization in the energy of the involved O 2p orbitals (Figure 6c). While the states of the unprotonated oxide ions remain largely unchanged, O−H bond formation leads to a distinct deep state stemming from the O 2p and H 1s overlaps at ≈−13 eV. The O−H bond formation leads also to a downward shift in the O 2p states of the respective O ion that are not directly involved in the O−H bond.

In addition to the covalent OH bond, the proton establishes two weaker hydrogen bonds with adjacent oxide ions. The structural motif of a protonic defect with one covalent and two hydrogen bonds is shown as the inset in Figure 7. With increasing oxygen deficiency and an increased Mulliken charge, the covalent OH bond shows a subtle but systematic increase in bond length (Figure 7a). The shorter hydrogen bond, in turn, shows a decrease in distance. Regarding the longer hydrogen bond, no clear trend is visible (Figure 7b). The longer hydrogen bond represents a comparably weak interaction and thus also depends on the overall geometry, which may be more influential than the correlation with the covalent O−H length. The bond length evolution shown in Figure 7 suggests that a longer covalent OH bond is compensated by stronger hydrogen bonding. The bonding patterns of protonated $(Ba,Sr)FeO_{3-\delta}$ are very similar (Figure S7).

The hydration energies E_{hydr} calculated for $BaFeO_{3-\delta}$ and $Ba_{0.5}Sr_{0.5}FeO_{3-\delta}$ relative to the respective unhydrated cells (averaged over the three lowest-energy configurations) are displayed in Figure 8. There is a correlation between the hydration energy and the oxygen stoichiometry, with values ranging from ≈−0.2 eV in the fully oxidized to ≈−1 eV in the reduced $BaFeO_{3-\delta}$[b] and from ≈0.2 to ≈−0.4 eV in $Ba_{0.5}Sr_{0.5}FeO_{3-\delta}$. Since the hydration reaction (1) is a pure acid−base reaction in which the hole concentration in the crystal remains unaltered, such a correlation is not necessarily expected. We attribute this observation to the effect of holes on the oxide ions. As outlined in Section 3.1, ligand holes alter the properties of lattice oxide ions as evidenced by the nonideal thermodynamics of oxygen nonstoichiometry and the change in Mulliken atomic charges. In this regard, a more negative

https://dx.doi.org/10.1021/acs.jpcc.0c01924
J. Phys. Chem. C 2020, 124, 11780−11789

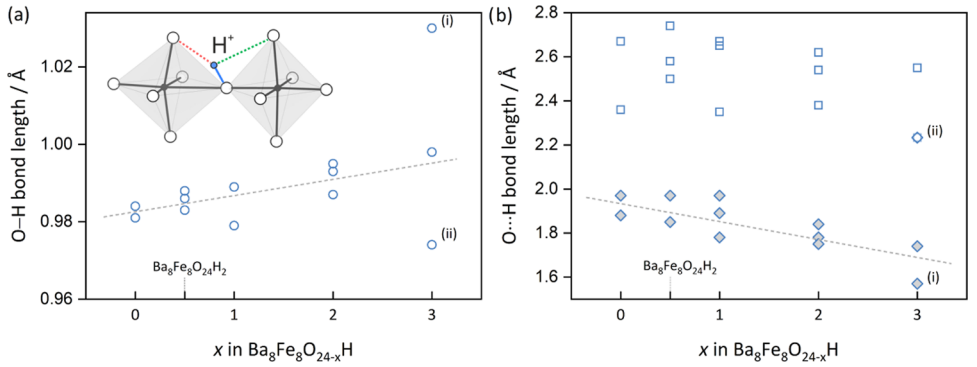

Figure 7. Bond length evolution of covalent OH and O···H hydrogen bondings in $Ba_8Fe_8O_{24-\delta}H$ for the three lowest-energy configurations. (a) Covalent OH bond ((i) only one very short hydrogen bond is present, leading to a longer covalent OH bond. (ii) Symmetric, longer hydrogen bonds leading to a shorter covalent OH bond). (b) Shorter and longer hydrogen bonds.

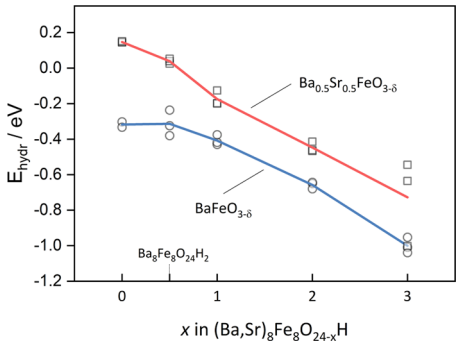

Figure 8. Hydration energy as a function of oxygen stoichiometry for $(Ba,Sr)_8Fe_8O_{24-x}H$. The lines represent the average of the three lowest-energy configurations.

oxygen atomic charge favors the stabilization of protons and leads to more negative hydration energies of higher oxygen deficiency (however, this simplistic relation is only valid within a certain perovskite system, since the fully oxidized $Ba_{0.5}Sr_{0.5}FeO_3$ has approximately the same oxygen ion charge as $BaFeO_3$ but exhibits a less negative hydration energy). The largely delocalized character of the holes in the O 2p bands has the consequence that even a low hole concentration already affects the hydration energy (in difference to a situation with strictly localized holes). The dependence of E_{hydr} on hole concentration leads to the pronounced anticorrelation of the proton and hole concentration in $(Ba,Sr)FeO_{3-\delta}$ and related PCFC cathode materials, which is much stronger than just the competition of positive defects in the electroneutrality condition.

The trends reported in the present study are in qualitative agreement with the experimental results,[13,30,63] which show a less negative hydration enthalpy for the higher formal Fe oxidation state, i.e., a higher concentration of holes. The slope in Figure 8 corresponds to a change in E_{hydr} of 0.8 eV between hole concentrations of 0 and 1. Experimentally, the E_{hydr} of $Ba_{0.85}La_{0.15}FeO_{3-\delta}$ varies by 0.35 eV (applying a defect model with the linear dependence of E_{hydr} on hole concentration; cf. Section 3.3).[63] The calculated hydration energies for reduced $BaFeO_{2.56}$ and $Ba_{0.5}Sr_{0.5}FeO_{2.56}$ agree with the experimental values of ≈−0.6 eV for $Ba_{0.95}La_{0.05}FeO_{2.525}$, ≈−0.9 eV for $Ba_{0.95}La_{0.05}Fe_{0.8}Zn_{0.2}O_{2.425}$, and ≈−0.6 eV for $Ba_{0.5}Sr_{0.5}FeO_{2.5}$.[13,13] Also, the finding of more negative hydration energies compared to that of $(La,Sr)FeO_{3-\delta}$[17] agrees with the experiments.

The dissociative absorption of water into oxygen vacancies is commonly associated with a chemical expansion of the solid oxide. The degree of expansion varies within different perovskites, ranging from 12 vol % percent in Y-doped $BaZrO_3$ per filled $V_O^{\bullet\bullet}$ and formula unit[67] to 16 vol % percent in $La_{0.5}Sr_{0.5}FeO_{3-\delta}$.[17,17] In $(Ba,Sr)FeO_{3-\delta}$, the chemical expansion upon hydration has a rather large scatter between different supercell configurations or between supercells of different oxygen stoichiometries (Figure 9), but no particular trend with

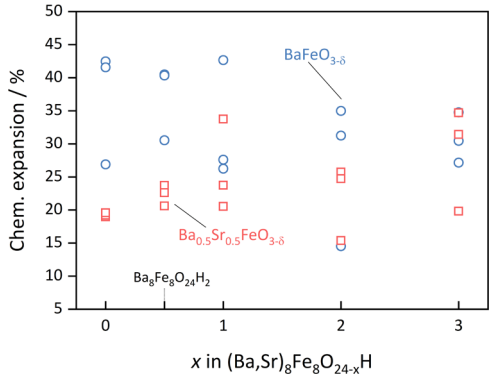

Figure 9. Chemical expansion upon hydration, i.e., volume increase per filling of one $V_O^{\bullet\bullet}$ per formula unit by H_2O (the volume of the respective unhydrated material has been averaged over the three lowest-energy configurations).

hole concentration is observed. Considering that most of the expansion originates from the filling of a $V_O^{\bullet\bullet}$ by a hydroxide ion in a pure acid−base reaction,[68] it is not surprising that this expansion shows no clear dependence on hole concentration. The values of the chemical expansion of 15−43 vol % in $BaFeO_3$ and 15−35 vol % in $Ba_{0.5}Sr_{0.5}FeO_3$ per filling of one $V_O^{\bullet\bullet}$ per formula unit by H_2O are significantly larger than for Y-doped $BaZrO_3$ and $La_{0.5}Sr_{0.5}FeO_{3-\delta}$.

3.3. Approaches for Defect Chemical Models.

The variation of $E_{V_O^{\bullet\bullet}}$ and E_{hydr} with hole concentration (Figures 5 and 8) represents deviations from ideally dilute defect chemistry. Experimental dependencies of $E_{V_O^{\bullet\bullet}}$ on hole concentration have been reported for several oxides, showing that at high hole concentration, further oxygen uptake is disfavored. This shows up in the partial molar enthalpy of oxygen, e.g., for $(La,Sr)CrO_{3-\delta}$ and $(La,Sr)CoO_{3-\delta}$, which decreases approximately linearly with increasing hole concen-

https://dx.doi.org/10.1021/acs.jpcc.0c01924
J. Phys. Chem. C 2020, 124, 11780−11789

tration.[69,70] If entropic contributions to the nonideality are negligible, this corresponds to a defect chemical model in which the reaction enthalpy changes linearly with hole concentration. For $La_2NiO_{4+\delta}$ and Na_xCoO_2, a model was suggested in which the nonideality is expressed by a hole activity coefficient exceeding unity,[71−73] which was further related to the Fermi−Dirac integral. Data for $La_2NiO_{4+\delta}$ were successfully modeled by both approaches.[71,74]

To the best of our knowledge, the experimental data in refs 12, 13, 63 are the first reports of E_{hydr} becoming less negative in the presence of holes. This nonideality differs from the nonidealities in unprotonated oxides by the fact that holes do not directly appear in the hydration reaction (eq 1); thus, this behavior cannot simply be quantified by a nonunity hole activity coefficient. The present DFT results indicate that the hole−hole and hole−proton nonidealities are closely related phenomena and that holes affect the hydration reaction by being largely delocalized to the oxygen ions. Quantitative defect chemical modeling for the variation of E_{hydr} (experimental and DFT results) with hole concentration for $(Ba,Sr,La)(Fe,Y,Zn)O_{3-\delta}$ will be discussed in more detail in a separate publication.

3.4. Conclusions. In the present study, we lay out a consistent picture of how p-type electronic conductivity and nonideal defect chemistry in $(Ba,Sr)FeO_{3-\delta}$ are both governed by delocalized ligand holes. An oxygen-to-metal charge transfer gives rise to electron holes in the O 2p valence band and results in a lower oxide ion charge.

The formation energy of an oxygen vacancy $E_{V_O^{\bullet\bullet}}$ increases with increasing oxygen nonstoichiometry, which represents a nonideal behavior. This could be attributed to the more delocalized character of the ligand holes affecting several oxide ions instead of a single Fe ion. Equivalently, it can be rationalized by a higher Fermi level in reduced $(Ba,Sr)FeO_{3-\delta}$ at which electrons remaining in the lattice from the removed oxide ions have to be accommodated.

Dissociative water absorption into oxygen vacancies becomes more favorable with increasing oxygen deficiency. The calculated hydration energy E_{hydr} spans a wide range from ≈−0.2 eV in the fully oxidized $BaFeO_3$ to ≈−1 eV in the reduced $BaFeO_{2.5}$ and from ≈0.2 to ≈−0.4 eV in $Ba_{0.5}Sr_{0.5}FeO_{3-\delta}$. This highlights the importance of the redox activity of the oxide ions in these materials. The more favorable hydration in the reduced $(Ba,Sr)FeO_{3-\delta}$ can at least in part be related to the more negatively charged oxide ions.

The reported dependencies of $E_{V_O^{\bullet\bullet}}$ and E_{hydr} on the concentration of electron holes are in qualitative agreement with the experimental studies showing that the present methodology is a reasonable approximation. The combination of electronic structure analysis and defect chemical discussion provides a deeper understanding of the observed trends, which is key for the further development of mixed proton electron conductors.

■ ASSOCIATED CONTENT

Supporting Information

The Supporting Information is available free of charge at https://pubs.acs.org/doi/10.1021/acs.jpcc.0c01924.

Evaluation of U_{eff}, Mulliken charges, O_2 energy correction, table of supercell configurations, analysis of $V_O^{\bullet\bullet}$−$V_O^{\bullet\bullet}$ interaction, Fe−O bond length distribution, band alignment procedure, and OH and O···H bond lengths for $Ba_4Sr_4Fe_8O_{24-x}H$, $E_{V_O^{\bullet\bullet}}$, and E_{hydr} for all configurations (PDF)

■ AUTHOR INFORMATION

Corresponding Author

R. Merkle − *Max Planck Institute for Solid State Research, Stuttgart 70569, Germany;* orcid.org/0000-0003-3811-8963; Email: r.merkle@fkf.mpg.de

Authors

M. F. Hoedl − *Max Planck Institute for Solid State Research, Stuttgart 70569, Germany;* orcid.org/0000-0003-3166-6772

D. Gryaznov − *Institute of Solid State Physics, University of Latvia, Riga LV-1586, Latvia;* orcid.org/0000-0002-2894-4471

E. A. Kotomin − *Max Planck Institute for Solid State Research, Stuttgart 70569, Germany; Institute of Solid State Physics, University of Latvia, Riga LV-1586, Latvia*

J. Maier − *Max Planck Institute for Solid State Research, Stuttgart 70569, Germany*

Complete contact information is available at: https://pubs.acs.org/10.1021/acs.jpcc.0c01924

Notes

The authors declare no competing financial interest.

■ ACKNOWLEDGMENTS

Financial support by the German−Israeli Foundation for Scientific Research and Development (grant I-1342-302.5/2016) and the Latvian Council of Science (grant lzp-2018/1-0147 (D.G., E.A.K.)) is gratefully acknowledged. The authors further thank Guntars Zvejnieks for help with CRYSTAL code calculations.

■ ADDITIONAL NOTES

[a]The presence or absence of JT distortions is also sensitive with regard to the computational details of the calculations. The balance between the cubic and JT distorted structures was shown to be dependent on the employed exchange−correlation functional.[58]

[b]The apparently decreased slope between $BaFeO_{3-\delta}$ $O_{24}H$ and $O_{24}H_2$ might be related to an overestimation of the energetic stabilization by Jahn−Teller-like distortions in the O24H configurations.

■ REFERENCES

(1) Duan, C.; Tong, J.; Shang, M.; Nikodemski, S.; Sanders, M.; Ricote, S.; Almansoori, A.; O'Hayre, R. Readily processed protonic ceramic fuel cells with high performance at low temperatures. *Science* **2015**, *349*, 1321−1326.

(2) Bae, K.; Jang, D. Y.; Choi, H. J.; Kim, D.; Hong, J.; Kim, B.-K.; Lee, J.-H.; Son, J.-W.; Shim, J. H. Demonstrating the potential of yttrium-doped barium zirconate electrolyte for high-performance fuel cells. *Nat. Commun.* **2017**, *8*, No. 14553.

(3) Choi, S.; Kucharczyk, C. J.; Liang, Y.; Zhang, X.; Takeuchi, I.; Ji, H.-I.; Haile, S. M. Exceptional power density and stability at intermediate temperatures in protonic ceramic fuel cells. *Nat. Energy* **2018**, *3*, 202−210.

(4) An, H.; Lee, H.-W.; Kim, B.-K.; Son, J.-W.; Yoon, K. J.; Kim, H.; Shin, D.; Ji, H.-I.; Lee, J.-H. A 5 × 5 cm^2 protonic ceramic fuel cell with a power density of 1.3 W cm^{-2} at 600 °C. *Nat. Energy* **2018**, *3*, 870−875.

(5) Xia, Y.; Jin, Z.; Wang, H.; Gong, Z.; Lv, H.; Peng, R.; Liu, W.; Bi, L. A novel cobalt-free cathode with triple-conduction for proton-conducting solid oxide fuel cells with unprecedented performance. *J. Mater. Chem. A* **2019**, *7*, 16136−16148.
(6) Merkle, R.; Poetzsch, D.; Maier, J. Oxygen Reduction Reaction at Cathodes on Proton Conducting Oxide Electrolytes: Contribution from Three Phase Boundary Compared to Bulk Path. *ECS Trans.* **2015**, *66*, 95−102.
(7) Han, D.; Okumura, Y.; Nose, Y.; Uda, T. Synthesis of $La_{1-x}Sr_xSc_{1-y}Fe_yO_{3-\delta}$ (LSSF) and measurement of water content in LSSF, LSCF and LSC hydrated in wet artificial air at 300 °C. *Solid State Ionics* **2010**, *181*, 1601−1606.
(8) Hashimoto, D.; Han, D.; Uda, T. Dependence of lattice constant of Ba, Co-contained perovskite oxides on atmosphere, and measurements of water content. *Solid State Ionics* **2014**, *262*, 687−690.
(9) Strandbakke, R.; Cherepanov, V. A.; Zuev, A. Y.; Tsvetkov, D. S.; Argirusis, C.; Sourkouni, G.; Prünte, S.; Norby, T. Gd- and Pr-based double perovskite cobaltites as oxygen electrodes for proton ceramic fuel cells and electrolyser cells. *Solid State Ionics* **2015**, *278*, 120−132.
(10) Vøllestad, E.; Schrade, M.; Segalini, J.; Strandbakke, R.; Norby, T. Relating defect chemistry and electronic transport in the double perovskite $Ba_{1-x}Gd_{0.8}La_{0.2+x}Co_2O_{6-\delta}$ (BGLC). *J. Mater. Chem. A* **2017**, *5*, 15743−15751.
(11) Poetzsch, D.; Merkle, R.; Maier, J. Proton conductivity in mixed-conducting BSFZ perovskite from thermogravimetric relaxation. *Phys. Chem. Chem. Phys.* **2014**, *16*, 16446.
(12) Zohourian, R.; Merkle, R.; Maier, J. Proton uptake into the protonic cathode material $BaCo_{0.4}Fe_{0.4}Zr_{0.2}O_{3-\delta}$ and comparison to protonic electrolyte materials. *Solid State Ionics* **2017**, *299*, 64−69.
(13) Zohourian, R.; Merkle, R.; Raimondi, G.; Maier, J. Mixed-Conducting Perovskites as Cathode Materials for Protonic Ceramic Fuel Cells: Understanding the Trends in Proton Uptake. *Adv. Funct. Mater.* **2018**, *28*, No. 1801241.
(14) Poetzsch, D.; Merkle, R.; Maier, J. Proton uptake in the H^+-SOFC cathode material $Ba_{0.5}Sr_{0.5}Fe_{0.8}Zn_{0.2}O_{3-\delta}$: transition from hydration to hydrogenation with increasing oxygen partial pressure. *Faraday Discuss.* **2015**, *182*, 129−143.
(15) Poetzsch, D.; Merkle, R.; Maier, J. Stoichiometry Variation in Materials with Three Mobile Carriers - Thermodynamics and Transport Kinetics Exemplified for Protons, Oxygen Vacancies, and Holes. *Adv. Funct. Mater.* **2015**, *25*, 1542−1557.
(16) Kreuer, K. Proton-Conducting Oxides. *Annu. Rev. Mater. Res.* **2003**, *33*, 333−359.
(17) Gryaznov, D.; Merkle, R.; Kotomin, E. A.; Maier, J. Ab initio modelling of oxygen vacancies and protonic defects in $La_{1-x}Sr_xFeO_{3-\delta}$ perovskite solid solutions. *J. Mater. Chem. A* **2016**, *4*, 13093−13104.
(18) Muñoz-García, A. B.; Tuccillo, M.; Pavone, M. Computational design of cobalt-free mixed proton−electron conductors for solid oxide electrochemical cells. *J. Mater. Chem. A* **2017**, *5*, 11825−11833.
(19) Wang, Z.; Yang, W.; Shafi, S. P.; Bi, L.; Wang, Z.; Peng, R.; Xia, C.; Liu, W.; Lu, Y. A high performance cathode for proton conducting solid oxide fuel cells. *J. Mater. Chem. A* **2015**, *3*, 8405−8412.
(20) Tan, W.; Huan, D.; Yang, W.; Shi, N.; Wang, W.; Peng, R.; Wu, X.; Lu, Y. A first-principles study on divergent reactions of using a $Sr_3Fe_2O_7$ cathode in both oxygen ion conducting and proton conducting solid oxide fuel cells. *RSC Adv.* **2018**, *8*, 26448−26460.
(21) Coulaud, E.; Dezanneau, G.; Geneste, G. Hydration, oxidation, and reduction of $GdBaCo_2O_{5.5}$ from first-principles. *J. Mater. Chem. A* **2015**, *3*, 23917−23929.
(22) Das, T.; Nicholas, J.; Qi, Y. Long-range charge transfer and oxygen vacancy interactions in strontium ferrite. *J. Mater. Chem. A* **2017**, *5*, 4493−4506.
(23) Das, T.; Nicholas, J.; Qi, Y. Polaron size and shape effects on oxygen vacancy interactions in lanthanum strontium ferrite. *J. Mater. Chem. A* **2017**, *5*, 25031−25043.
(24) Kotomin, E.; Mastrikov, Y.; Kuklja, M.; Merkle, R.; Roytburd, A.; Maier, J. First principles calculations of oxygen vacancy formation and migration in mixed conducting $Ba_{0.5}Sr_{0.5}Co_{1-y}Fe_yO_{3-\delta}$ perovskites. *Solid State Ionics* **2011**, *188*, 1−5.
(25) Bjørheim, T.; Hoedl, M.; Merkle, R.; Kotomin, E.; Maier, J. Proton, Hydroxide Ion, and Oxide Ion Affinities of Closed-Shell Oxides: Importance for the Hydration Reaction and Correlation to Electronic Structure. *J. Phys. Chem. C* **2019**, *124*, 1277−1284.
(26) Bocquet, A. E.; Fujimori, A.; Mizokawa, T.; Saitoh, T.; Namatame, H.; Suga, S.; Kimizuka, N.; Takeda, Y.; Takano, M. Electronic structure of $SrFe_4O_3$ and related Fe perovskite oxides. *Phys. Rev. B* **1992**, *45*, 1561−1570.
(27) Tsuyama, T.; Matsuda, T.; Chakraverty, S.; Okamoto, J.; Ikenaga, E.; Tanaka, A.; Mizokawa, T.; Hwang, H. Y.; Tokura, Y.; Wadati, H. X-ray spectroscopic study of $BaFeO_3$ thin films: An Fe^{4+} ferromagnetic insulator. *Phys. Rev. B* **2015**, *91*, No. 115101.
(28) Abbate, M.; Zampieri, G.; Okamoto, J.; Fujimori, A.; Kawasaki, S.; Takano, M. X-ray absorption of the negative charge-transfer material $SrFe_{1-x}Co_xO_3$. *Phys. Rev. B* **2002**, *65*, No. 165120.
(29) Mizumaki, M.; Fujii, H.; Yoshii, K.; Hayashi, N.; Saito, T.; Shimakawa, Y.; Uozumi, T.; Takano, M. Electronic structure of $BaFeO_3$ studied by X-ray spectroscopy. *Phys. Status Solidi C* **2015**, *12*, 818−821.
(30) Zohourian, R.; Merkle, R.; Maier, J. Bulk Defect Chemistry of PCFC Cathode Materials: Discussion of Defect Interactions. *ECS Trans.* **2017**, *77*, 133−138.
(31) Kresse, G.; Hafner, J. Ab-initio molecular dynamics for liquid metals. *Phys. Rev. B* **1993**, *47*, 558−561.
(32) Kresse, G.; Furthmüller, J. Efficiency of ab-initio total energy calculations for metals and semiconductors using a plane-wave basis set. *Comput. Mater. Sci.* **1996**, *6*, 15−50.
(33) Kresse, G.; Furthmüller, J. Efficient iterative schemes for ab-initio total-energy calculations using a plane-wave basis set. *Phys. Rev. B* **1996**, *54*, 11169−11186.
(34) Blöchl, P. E. Projector augmented-wave method. *Phys. Rev. B* **1994**, *50*, 17953−17979.
(35) Kresse, G.; Joubert, D. From ultrasoft pseudopotentials to the projector augmented-wave method. *Phys. Rev. B* **1999**, *59*, 1758−1775.
(36) Monkhorst, H. J.; Pack, J. D. Special points for Brillouin-zone integrations. *Phys. Rev. B* **1976**, *13*, 5188−5192.
(37) Perdew, J. P.; Burke, K.; Ernzerhof, M. Generalized Gradient Approximation Made Simple. *Phys. Rev. Lett.* **1996**, *77*, 3865−3868.
(38) Dudarev, S.; Botton, G.; Savrasov, S.; Humphreys, C.; Sutton, A. Electron-energy-loss spectra and the structural stability of nickel oxide: An LSDA+U study. *Phys. Rev. B* **1998**, *57*, 1505−1509.
(39) Ribeiro, B.; Godinho, M.; Cardoso, C.; Borges, R.; Gasche, T. Self-doping and the role of oxygen vacancies in the magnetic properties of cubic $BaFeO_{3-\delta}$. *J. Appl. Phys.* **2013**, *113*, No. 083906.
(40) Lee, Y.; Kleis, J.; Rossmeisl, J.; Morgan, D. Ab initio energetics of $LaBO_3$ (001) (B= Mn, Fe, Co, and Ni) for solid oxide fuel cell cathodes. *Phys. Rev. B* **2009**, *80*, No. 224101.
(41) Baiyee, Z.; Chen, C.; Ciucci, F. A DFT+U study of A-site and B-site substitution in $BaFeO_{3-\delta}$. *Phys. Chem. Chem. Phys.* **2015**, *17*, 23511−23520.
(42) Okhotnikov, K.; Charpentier, T.; Cadars, S. Supercell program: a combinatorial structure-generation approach for the local-level modeling of atomic substitutions and partial occupancies in crystals. *J. Cheminf.* **2016**, *8*, 17.
(43) Dronskowski, R.; Blöchl, P. E. Crystal orbital Hamilton populations (COHP): energy-resolved visualization of chemical bonding in solids based on density-functional calculations. *J. Phys. Chem. A* **1993**, *97*, 8617−8624.
(44) Deringer, V. L.; Tchougréeff, A. L.; Dronskowski, R. Crystal orbital Hamilton population (COHP) analysis as projected from plane-wave basis sets. *J. Phys. Chem. A* **2011**, *115*, 5461−5466.
(45) Maintz, S.; Deringer, V. L.; Tchougréeff, A. L.; Dronskowski, R. Analytic projection from plane-wave and PAW wavefunctions and application to chemical-bonding analysis in solids. *J. Comput. Chem.* **2013**, *34*, 2557−2567.
(46) Maintz, S.; Deringer, V. L.; Tchougréeff, A. L.; Dronskowski, R. LOBSTER: A tool to extract chemical bonding from plane-wave based DFT. *J. Comput. Chem.* **2016**, *37*, 1030−1035.

https://dx.doi.org/10.1021/acs.jpcc.0c01924
J. Phys. Chem. C 2020, 124, 11780−11789

(47) Ertural, C.; Steinberg, S.; Dronskowski, R. Development of a robust tool to extract Mulliken and Löwdin charges from plane waves and its application to solid-state materials. *RSC Adv.* **2019**, *9*, 29821−29830.
(48) Mori, S. Preparation of Various Phases of $BaFeO_{3-x}$. *J. Am. Ceram. Soc.* **1965**, *48*, 165.
(49) Mori, S. Phase Transformation in Barium Orthoferrate, $BaFeO_{3-x}$. *J. Am. Ceram. Soc.* **1966**, *49*, 600−605.
(50) Parras, M.; Fournes, L.; Grenier, J. C.; Pouchard, M.; Vallet, M.; Calbet, J.; Hagenmuller, P. Structural aspects and Mössbauer resonance investigation of $Ba_2Fe_2O_5$. *J. Solid State Chem.* **1990**, *88*, 261−268.
(51) Zou, X.; Hovmöller, S.; Parras, M.; Gonzalez-Calbet, J.; Vallet-Regi, M.; Grenier, J. The complex perovskite-related superstructure $Ba_2Fe_2O_5$ solved by HREM and CIP. *Acta Crystallogr., Sect. A: Found. Crystallogr.* **1993**, *49*, 27−35.
(52) Parras, M.; Gonzales-Calbet, J.; Valletregi, M.; Grenier, J. A high temperature study of the $BaFeO_{3-y}$ system. *Solid State Ionics* **1993**, *63*−*65*, 714−718.
(53) Hayashi, N.; Yamamoto, T.; Kageyama, H.; Nishi, M.; Watanabe, Y.; Kawakami, T.; Matsushita, Y.; Fujimori, A.; Takano, M. $BaFeO_3$: a ferromagnetic iron oxide. *Angew. Chem., Int. Ed.* **2011**, *50*, 12547−12550.
(54) Chen, C.; Chen, D.; Gao, Y.; Shao, Z.; Ciucci, F. Computational and experimental analysis of $Ba_{0.95}La_{0.5}FeO_{3-\delta}$ as a cathode material for solid oxide fuel cells. *J. Mater. Chem. A* **2014**, *2*, 14154−14163.
(55) Zhu, X.; Wang, H.; Yang, W. Structural stability and oxygen permeability of cerium lightly doped $BaFeO_{3-\delta}$ ceramic membranes. *Solid State Ionics* **2006**, *177*, 2917−2921.
(56) Hayashi, N.; Yamamoto, T.; Kitada, A.; Matsuo, A.; Kindo, K.; Hester, J.; Kageyama, H.; Takano, M. Field-Induced Ferromagnetism of Fe^{4+}-Perovskite System, $Sr_{1-x}Ba_xFeO_3$ ($0 \leq x \leq 1$). *J. Phys. Soc. Jpn.* **2013**, *82*, No. 113702.
(57) MacChesney, J.; Sherwood, R.; Potter, J. Electric and magnetic properties of the strontium ferrates. *J. Chem. Phys.* **1965**, *43*, 1907−1913.
(58) Cherair, I.; Bousquet, E.; Schmitt, M.; Iles, N.; Kellou, A. First-principles study of strain-induced Jahn-Teller distortions in $BaFeO_3$. *J. Phys.: Condens. Matter* **2018**, *30*, No. 255701.
(59) Wang, L.; Merkle, R.; Cristiani, G.; Stuhlhofer, B.; Habermeier, H.; Maier, J. PLD-deposited $(Ba_xSr_{1-x})(Co_yFe_{1-y})O_{3-\delta}$ Thin-Film Microelectrodes: Structure Aspects and Oxygen Incorporation Kinetics. *ECS Trans.* **2008**, *13*, 85−95.
(60) Vračar, M.; Kuzmin, A.; Merkle, R.; Purans, J.; Kotomin, E.; Maier, J.; Mathon, O. JahnTeller distortion around Fe^{4+} in $Sr(Fe_xTi_{1-x})O_{3-\delta}$ from X-ray absorption spectroscopy, X-ray diffraction, and vibrational spectroscopy. *Phys. Rev. B* **2007**, *76*, No. 174107.
(61) Lein, H.; Wiik, K.; Grande, T. Thermal and chemical expansion of mixed conducting $La_{0.5}Sr_{0.5}Fe_{1-x}Co_xO_{3-\delta}$ materials. *Solid State Ionics* **2006**, *177*, 1795−1798.
(62) Jedvik, E.; Lindman, A.; Benediktsson, M. P.; Wahnström, G. Size and shape of oxygen vacancies and protons in acceptor-doped barium zirconate. *Solid State Ionics* **2015**, *275*, 2−8.
(63) Zohourian, R. Mixed-Conducting Perovskites as Cathodes in Protonic Ceramic Fuel Cells: Defect Chemistry and Transport Properties. Ph.D. thesis, University of Stuttgart, 2018.
(64) Lee, Y. L.; Kleis, J.; Rossmeisl, J.; Shao-Horn, Y.; Morgan, D. Prediction of solid oxide fuel cell cathode activity with first-principles descriptors. *Energy Environ. Sci.* **2011**, *4*, 3966−3970.
(65) Lankhorst, M.; Bouwmeester, H.; Verweij, H. Use of the rigid band formalism to interpret the relationship between O chemical potential and electron concentration in $La_{1-x}Sr_xCoO_{3-\delta}$. *Phys. Rev. Lett.* **1996**, *77*, 2989.
(66) Hoedl, M.; Makagon, E.; Lubomirsky, I.; Merkle, R.; Kotomin, E.; Maier, J. Impact of point defects on the elastic properties of $BaZrO_3$: Comprehensive insight from experiments and ab initio calculations. *Acta Mater.* **2018**, *160*, 247−256.
(67) Bjørheim, T.; Kotomin, E.; Maier, J. Hydration entropy of $BaZrO_3$ from first principles phonon calculations. *J. Mater. Chem. A* **2015**, *3*, 7639−7648.
(68) Bjørheim, T. S.; Løken, A.; Haugsrud, R. On the relationship between chemical expansion and hydration thermodynamics of proton conducting perovskites. *J. Mater. Chem. A* **2016**, *4*, 5917−5924.
(69) Mizusaki, J.; Yamauchi, S.; Fueki, K.; Ishikawa, A. Non-stoichiometry of the perovskite-type oxide $La_{1-x}Sr_xCrO_{3-\delta}$. *Solid State Ionics* **1984**, *12*, 119−124.
(70) Mizusaki, J.; Mima, Y.; Yamauchi, S.; Fueki, K.; Tagawa, H. Nonstoichiometry of the perovskite-type oxides $La_{1-x}Sr_xCoO_{3-\delta}$. *J. Solid State Chem.* **1989**, *80*, 102−111.
(71) Kim, H.-S.; Yoo, H.-I. Defect-chemical analysis of the nonstoichiometry, conductivity and thermopower of $La_2NiO_{4+\delta}$. *Phys. Chem. Chem. Phys.* **2010**, *12*, 4704−4713.
(72) Kim, H.-S.; Yoo, H.-I. On the origin of positive deviation of the defect structure of complex oxides. *Solid State Ionics* **2012**, *229*, 59−73.
(73) Joo, W.; Yoo, H.-I. Point defect structure of γ-Na_xCoO_2. *Solid State Ionics* **2018**, *314*, 74−80.
(74) Nakamura, T.; Yashiro, K.; Sato, K.; Mizusaki, J. Oxygen nonstoichiometry and defect equilibrium in $La_{2-x}Sr_xNiO_{4+\delta}$. *Solid State Ionics* **2009**, *180*, 368−376.

This paper is elaborated at the Centre of Excellence in Advanced Material Research and Technology Transfer of the Institute of Solid State Physics, University of Latvia executing project CAMART² that has received funding from the Horizon 2020 Framework Programme H2020-WIDESPREAD-01-2016-2017-TeamingPhase2 under grant agreement No. 739508

https://dx.doi.org/10.1021/acs.jpcc.0c01924
J. Phys. Chem. C 2020, 124, 11780−11789